

Generation of internal tidal beam in Tasman Sea

July 13, 2018

Abstract

Macquarie Ridge south of New Zealand is a strong generator of internal tidal waves (ITs) which later form a prominent internal tidal beam, a tight filament of baroclinic tidal energy. The mechanism of barotropic energy conversion into baroclinic field is investigated by means of numerical experiments with prescribed mesoscale conditions corresponding to different background conditions. The obtained energy transfer rates into IT mode-1 show variability both in its magnitude and spatial distribution. This variability is controlled by resonance between local barotropic forcing and remotely generated ITs. The remote baroclinic signal takes its origin at an easterly located Campbell Plateau. Their pathway is drastically different from the progressive plane waves due to interference with the ridge originating waves and consequent formation of a standing Poincare wave. This complex internal tide environment is modulated by the ratio of the respective East and West traveling components. *The west part associated with the plateau experiences variability following the upper ocean stratification. (this currently questionable)* Under conditions of the Tasman Sea subtropical frontal zone located northward of the region, leading to weaker stratification, lower amplitude waves, a more developed standing wave and hence, less energy transfer into the internal tidal beam. Conversely, under different realization an intrusion of warm subtropical waters created conditions for stronger generation resulting in high across Macquarie ridge

energy transport and larger conversion rates. This mechanism of variability is further shown to affect position of the internal tidal beam. It is characterized by complex pattern of nodes and antinodes. The simple inverse analytical models shows that spatially wide-spread generation is one to blame. Then it is shown that the beam wobbles as a result in shifting of internal tide production hotspots. This identifies a reason for beam long range nonstationarity as a result of generation nonstationarity.

The inverse model based on elliptical waves shows that the beam undergoes changes in its appearance similar to Fresnel and Fraunhoffer diffraction in optics.

1 Introduction

Baroclinic semidiurnal tides originate as a strong barotropic flow occurs over steep topography in stratified ocean. This process is though as a scattering of barotropic tidal energy into baroclinic motions (Wunsch (1975)). It is quite definitely known that the scattering has a large impact on energetics barotropic tide and is a part of energy dissipation (Egbert and Ray (2000), Munk (1997)) with 1/3 of M_2 energy being dissipated through generation of internal tide.

Analytical models of internal tide generation points to importance of ratio between direction of internal wave characteristics to bathymetry slope (Garrett and Kunze (2007)). Omitting nonlinear regimes for low Froude number flows, highly supercritical slopes will give rise mostly to the gravest mode of internal tide (Echeverri and Peacock (2010)). Such a case for Macquarie Ridge located south of New Zealand. Here barotropic tide energy is converted into largely mode-1 baroclinic tide.

Variability of internal tide generation can occur to number of reasons. Stratification could have a direct impact in WKB sense creating less prominent obstacle (Holloway and Merrifield (1999)). But this phenomena is more pronounced for bathymetry touching pycnocline. More recently, it became apparent that the generation is more unstable in presence of remote

baroclinic signals. In the most well studied setting of two parallel ridges a resonance conditions occurs (Echeverri and Peacock (2010), Buijsman et al. (2012b), Buijsman et al. (2014)) that would lead either to intensification or destruction of energy transfers. More generally, phenomena of coupling at internal tide production sites of local generation and remote signal can lead to nonstationarity in wave generation (Kelly and Nash (2010), Osborne et al. (2011), Kerry et al. (2013), Xing and Davies (1998), Buijsman et al. (2012a)). The notion of variability in generation was observed as well (Pickering et al. (2015), Zilberman et al. (2011)). The same phenomena occurs at Macquarie Ridge where behind located Campbell Plateau sends internal tides which results in generation variability.

The ubiquitous feature of mode-1 internal tides as they leave production sites is their appearance as tightly confined beams of energy propagating without much spatial spreading over large distances (Zhao et al. (2016)). This surprising feature is believed to be related to multiple generation sites (Rainville et al. (2010), Terker et al. (2014)). Especially, this is true for long swaths of generation bathymetry where point source two dimensional models of generation becomes unrealistic (Munroe and Lamb (2005)).

The question of stationarity of the tidal beams is still open. The most obvious reason for variations is nonlinear interaction with variable mesoscale conditions in the open sea (Kerry et al. (2016), Dunphy and Lamb (2014), Chavanne et al. (2010), Ansong et al. (2017), Dunphy et al. (2017), Zaron and Egbert (2014), Mooers (1975), (Kelly and Lermusiaux, 2016), (Park and Watts, 2006), Rainville and Pinkel (2006)). On the first order, refraction by variable stratification and hence, propagation speed is a key processes or reflection at strong frontal zones. Oppositely, here we will provide analysis suggestive for a different point such that variable spatial conversion rates will lead to displacement of Tasman Sea tidal beam. This is done by investigation of numerical experiments in Regional Ocean Modeling System with different realistic background conditions (Section 2). From derived energy characteristics it is shown that variations occur both at generation regions (Section 3a), but also in open ocean (Section 3b). Then developed analytical solution for spatially confined knife-edge

barrier and semi-analytical solution (Section 3c) can describe the beam properties from pure generation picture. This provides rough estimates on generation-related nonstationarity. The work is concluded with inter-comparison between numerical experiments and available observational data (Section 4). In conclusion wide-spread application is provided (Section 5).

2 Numerical experiments and analysis

2.1 Numerical experiments

To study variability of internal tide generation around New Zealand and later propagation numerical simulations were carried out with Regional Ocean Modeling System (Shchepetkin and McWilliams, 2005). The numerical domain covered southern Tasman Sea from subantarctic waters of 60° S to subtropics in 35° S. And the zonal extent stretched from 142° to 172° E. This ensued correct representation of reach regional, oceanographic conditions. The horizontal grid spacing was taken to be of $1/32^{\circ}$ corresponding on average to discretization of 3 km in zonal direction and 2.5 km in meridional. The nonuniformly separated, vertical 50 *s*-levels were placed to smoothly follow subsurface terrain.

Such discretization of vertical momentum equation tends to induce artificial, horizontal along-slope flows (Haidvogel and Beckmann, 1999) due to errors in reproducing of pressure gradient force. Especially severe errors are made by steep terrain. The misbehavior is usually solved by aritificial smoothing of topography. Here this is done by spatial filtering¹. This procedure has an adverse effect on internal tide generation (Di Lorenzo et al., 2006) since production sites are found where bottom gradients are large. To test sensibility of numerical setup, a sensitivity study was carried out with simulations of $1/8^{\circ}$, $1/16^{\circ}$, $1/64^{\circ}$ horizontal resolution. The essential for this study internal tide behavior appeared at $1/16^{\circ}$ and converged for $1/32^{\circ}$ and $1/64^{\circ}$ cases where no marked difference was observed, except a substantial increase in high mode content which is in line with² (Di Lorenzo et al., 2006). This work addresses the gravest baroclinic mode dynamics in the deep ocean. Spatial extent of waves is large compared to associated vertical displacements. This ensures linear regime of propagation without dispersive and nonhydrostatic effects taken place such as fission into solitons. A hydrostatic solver used in ROMS seems to be a proper choice for the simulations. Such simplification in wave dynamics was assumed in previous studies ((Carter et al., 2008;

¹How it was done?

²previous investigations

Merrifield et al., 2001; Merrifield and Holloway, 2002; Kerry et al., 2013)). In the nonhydrostatic simulations (Kang and Fringer, 2012; Zhang et al., 2011) the nonhydrostatic effects are found to be important for shoaling internal tides, while for main part generation follows linear dynamics with vertical accelerations to have a negligible contribution.

Frictional forces

The horizontal boundary conditions were imposed to be open for depth-averaged, barotropic flows following³. The baroclinic fields are nudged to zero by linear increased lateral viscosity and diffusivity over sponge layers. Through the same outer boundaries numerical simulations were forced with barotropic tide. The tidal currents and sea level are derived from TPXO atlas, version 7.2 (Egbert and Erofeeva, 2002) and prescribed as linearly interpolated volume transports. It was used only the largest semidiurnal constituent M_2 . The amplitude ratio between the principal lunar and solar components are 4-to-1 suggestive of slight open-ocean spring-neap modulation. The diurnal species are weak in the region except shoals east of New Zealand (Walters et al., 2001)⁴.

To investigate variations of baroclinic tide dynamics several ocean states were prescribed and analyzed separately. In the simplest setting, no lateral gradients in water density were given and vertical gradient was representative of Tasman Sea basin climatological mean. The second set of simulations was comprised to investigate interannual and interseasonal variability (Table 1). And the third calculation was intended to provide context for TTIDE field program, so this was done by performing a single experiment once initialized and then let run for three numerical months. The simulations with variable conditions were at first initialized by HYCOM hindcasts⁵ for respective start date. Then during temporal integration, along with barotropic tidal flow, time-variable, subtidal two dimensional fields⁶ of horizontal currents, temperature and salinity were prescribed into the numerical ocean. The air-sea interaction was also given from MERRA-reanalysis (Rienecker et al., 2011) by

³Shchepetkin's condition, is there any reference?

⁴Do I need to justify M_2 only choice?

⁵cite?

⁶(vertical coordinate and along boundary coordinate)

Table 1: Carried out numerical experiments

Numerical experiments used in this study		
Experiment abbreviation	Dates	Comments (reason?)
Uniform		No mesoscale
2012	Jan 1st - Jan 15th, 2012	Interannual
2013	Jan 1st - Jan 15th, 2013	Interannual
2014	Jan 1st - Jan 15th, 2014	Interannual
2015	Jan 1st - Jan 15th, 2015	Interannual
2013_274	Oct 1st - Oct 15th, 2013	Interseaonal
2015_074	Mat 1st - Mar 15th, 2015	Interseaonal
2015_TTIDE	Jan 1st - Mar 1st, 2015	Field period

insolation, air temperature, EP rates and most importantly, wind stresses.

2.2 Internal tide analysis

As it is seen in table 1, the simulations were carried for 15 days or longer. The first 10 days were given for spin up of baroclinic tide generation and propagation. Roughly, it takes about 7 days for the mode-1 signal to cross Tasman Sea basin from New Zealanda to Tasmania. After that period, three dimensional fields velocity, temperature and salinity were sampled hourly. These were later subject to high pass filtering. Butterworth filter of order x with cut off time of 30 hours were applied to the records. This produced tidal signal that was further fit in a least square sense to the principle semidiurnal harmonic. Then the three dimensional fields was then underwent a routine separation of barotropic and baroclinic signals (Cummins and Oey, 1997; Kunze et al., 2002; Carter et al., 2008), depth-averaged current is thought to represent a pure barotropic signal and any vertical deviation is attributed to a baroclinic wave,

$$\vec{u}_{bt}(x, y) = \frac{1}{H} \int_{-H}^0 \vec{u}(x, y, z) dz, \quad \vec{u}_{bc}(x, y, z) = \vec{u}(x, y, z) - \vec{u}_{bt}(x, y) \quad (1)$$

To describe distribution of pressure at first, from a linear equation of state and respective TS-fields density perturbation from the reference is obtained. Then the hydrostatic approximation is employed and after vertical integration the total pressure fields is found. This is

then subject to barotropic condition, so that baroclinic field is taken to be as a deviation from the depth-averaged,

$$p(x, y, z) = \int_{-z}^0 \rho(x, y, z) dz, \quad p_{bc}(x, y) = p(x, y, z) - \frac{1}{H} \int_{-H(x,y)}^0 \rho(x, y, z) dz \quad (2)$$

In the both expressions rigid-lid approximation is used. This is a valid statement unless vertical accelerations are smaller than acceleration due to gravity which is true except shallow depths Kelly et al. (2010).

Each dynamical variable was then decomposed into vertical modes. The structure functions were obtained by using local Brunt-Vaisala frequency profiles found from averaged density fields. These were used in Sturm-Liouville problem for the hydrostatic approximation,

$$\frac{d}{dz} \left(\frac{\omega^2 - f^2}{N^2} \right) \frac{d\psi(z)}{dz} + c_n^2 \psi(z) = 0 \quad (3)$$

where c_n is a mode respective phase speed in nonrotating ocean. The first 3 vertical modes were fit three-dimensional fields. And only mode-1 was used in the Chapter.

Now energy diagnostics could be obtained. First, depth-averaged mode-1 energy flux will be simply,

$$\vec{F} = \frac{1}{2} \frac{1}{H} \vec{u}^* p \int_{-H}^0 \psi_1(z) \psi_1(z) dz \quad (4)$$

At second, rates of conversion from barotropic to baroclinic (Simmons et al., 2004; Kurapov et al., 2003) were calculated as,

$$C_{bt \rightarrow 1} = -\frac{1}{2} (\vec{u}_{bt}^* \cdot \nabla H) p_1 \quad (5)$$

The fraction $\frac{1}{2}$ in front of the energy characteristics appear because harmonic, complex amplitudes are used in the expressions.

These calculations had produced a set of dynamical variables related to barotropic and baroclinic fields in each experiment (table.1). The obtained values hereafter will be referred

as a realization. For instance, the longest experiment, 2015_TTIDE had 10 realizations which are all dependent since it was the continuous simulation. The latter calculation of stationarity was made by simple expressions,

2.3 Discrete Fourier Decomposition by inverse modeling

In addition to the above characteristics the mode-1 internal tide field was subject to directional analysis in order to remove interference modulations by a novel approach. Though similar methods were used previously in internal tide field programs (Hendry, 1977; Lozovatsky et al., 2003) that were based on array beamforming method and stationarity of the field or satellite altimetry (Dushaw, 2002) or in surface wave studies (Longuet-Higgins, 1961; Munk et al., 1963; Long, 1986). Let mode-1 pressure in complicated seas to be described by an angular spectrum

$$p(\vec{r}, t) = \int_0^{2\pi} d\theta_k S(\theta_k) e^{i\vec{k}(\theta_k) \cdot \vec{r} + \phi(\theta_k) - i\omega t} \quad (6)$$

Here each elementary (monochromatic) sine wave of wavenumber k travels in direction θ with energy $S(\theta)^2 d\theta$ and temporal (spatial) lag of $\phi(\theta)$. The statement can be reformulated in terms of Fourier coefficients (Munk et al., 1963) by application of Jacobi-Anger expansion,

$$p(r, \theta) = e^{i\vec{k}(\theta) \cdot \vec{r}} = \sum_{m=-\infty}^{m=\infty} i^m J_m(kr) e^{im(\theta - \theta_k)} \quad (7)$$

shows that a field at point (r, θ) produced by plane wave can be expanded in series of Bessel functions and circular functions. Then its substitution into (6) and reorganization lead to

$$p(r, \theta) = \sum_{m=-\infty}^{m=\infty} \left[\int_0^{2\pi} d\theta_k S(\theta_k) e^{i\phi(\theta_k)} e^{-im\theta_k} \right] i^m J_m(kr) e^{im\theta} \quad (8)$$

Term in brackets (square brackets) represent convolution integrals defining Fourier coefficients of order m , $A_m - iB_m$. Thence, series (8) state a model equation to find the unknown coefficients from the known, measured pressure field that were sampled at a set of points

(r_i, θ_i) and if infinite series is truncated at some order N . Real and imaginary parts will constitute two separate problems allowing deterministic definition of the spectrum.

The same steps are repeated but with current velocities instead. By invoking plane wave polarization relations (e.g., Müller and Liu, 2000) are inserted into (6) and the following equations are found,

$$\begin{Bmatrix} u_i \\ v_i \end{Bmatrix} = \frac{1}{2} \sum_{m=-N}^{m=N} J_m(kr_i) e^{im(\theta+\pi/2)} \begin{Bmatrix} (\omega - f)A_{m+1} + (\omega + f)A_{m-1} - i[(\omega - f)B_{m+1} + (\omega + f)B_{m-1}] \\ (\omega - f)B_{m+1} - (\omega + f)B_{m-1} + i[(\omega - f)A_{m+1} - (\omega + f)A_{m-1}] \end{Bmatrix} \quad (9)$$

The dependence of currents on wave bearing causes splitting of Fourier coefficients and asymmetry via Coriolis effect. This results points out that to describe velocity field higher circular harmonics have to be used. Physically, velocity field has higher spatial wavenumber. But in (9) additionally, the asymmetry is observed for clockwise and counterclockwise components. An inverse model combines dynamical relations of (??) and (9) into a matrix equation

$$y = Kx \quad (10)$$

Generally, it is unstable to small errors in data and produce physically inconsistent results. This can be avoided by seeking a damped least square solution (Munk et al., 2009) where minimization function is given by

$$J = \|Kx - y\|_2^2 + \alpha\|x\|_2^2 \quad (11)$$

The unknown regularization parameters acts as a high-pass filter (Williams, 2001). In field studies this is usually set by a signal-to-noise ratio (Munk et al. (2009)), since the parameter scales noise variance (residue) to actual signal's strength. To obtain α in data-driven way a straightforward approach is adapted that based on trade-off curve method (Hansen and

OLeary (1993)). In (11) amount of allowed error is competing with solution's variance. An optimal parameter should balance these factors. This is seen as a rapid change in behavior of curve associating residue with model's norm as regularization varie. In most cases the curve has a sharp corner connecting aforementioned limits, hence, the method's name is a L-curve (Hansen (1999)). And the corner is to occur for an optimal regularization parameter. The equations (8) and (9) are sampled at locations in a concentric arrays placed at λ , 0.5λ , 0.25λ where λ is a local mode-1 wavelength. At each location u , v , p are used as data and for a region embraced by array Fourier coefficients are found. And these then are used in reconstructions.

The method used here is different from (Zhao et al., 2010) for two main reasons. The model equations produce simultaneous fit of all the components, rather than a finite number of a single directed plane waves. This can make a difference in regions where diffraction is important such as near internal tide generation or scattering regions. And at second, velocity field is utilized which provides an additional constrain. Moreover, in synthetic experiments with (11) where instead of L_2 -norm regularization it was used L_1 -norm, the results were approaching one of plane wave technique of (Zhao et al., 2010). Additionally, the proposed method can be utilized for a single mooring where half-space separation is necessary.

3 Results

3.1 Ridge

3.2 Mid-basin beam

The mid basin properties of the tidal beam include:

- wobbling
- slightly increased phase speed

- large deviations of group speed
- wavefronts
- spotty APE and HKE

These properties point to use that the beam is a standing wave. But no apparent reflected wave is seen. Generation at Southern Tasman Plateau and Cascade Seamount can not be a source for opposite traveling waves due to their weakness. Additionally, directional spectra or plane wave fit does not show presence of such waves. But here we will show that generation indeed is responsible for wobbly pattern of the tidal beam and present a method that connects conversion pattern along Macquarie Ridge with mid basin characteristics of the beam.

Study the wavefield varies depending on size of the ridge.

3.3 Analytical results

4 Discussion

4.1 Generation

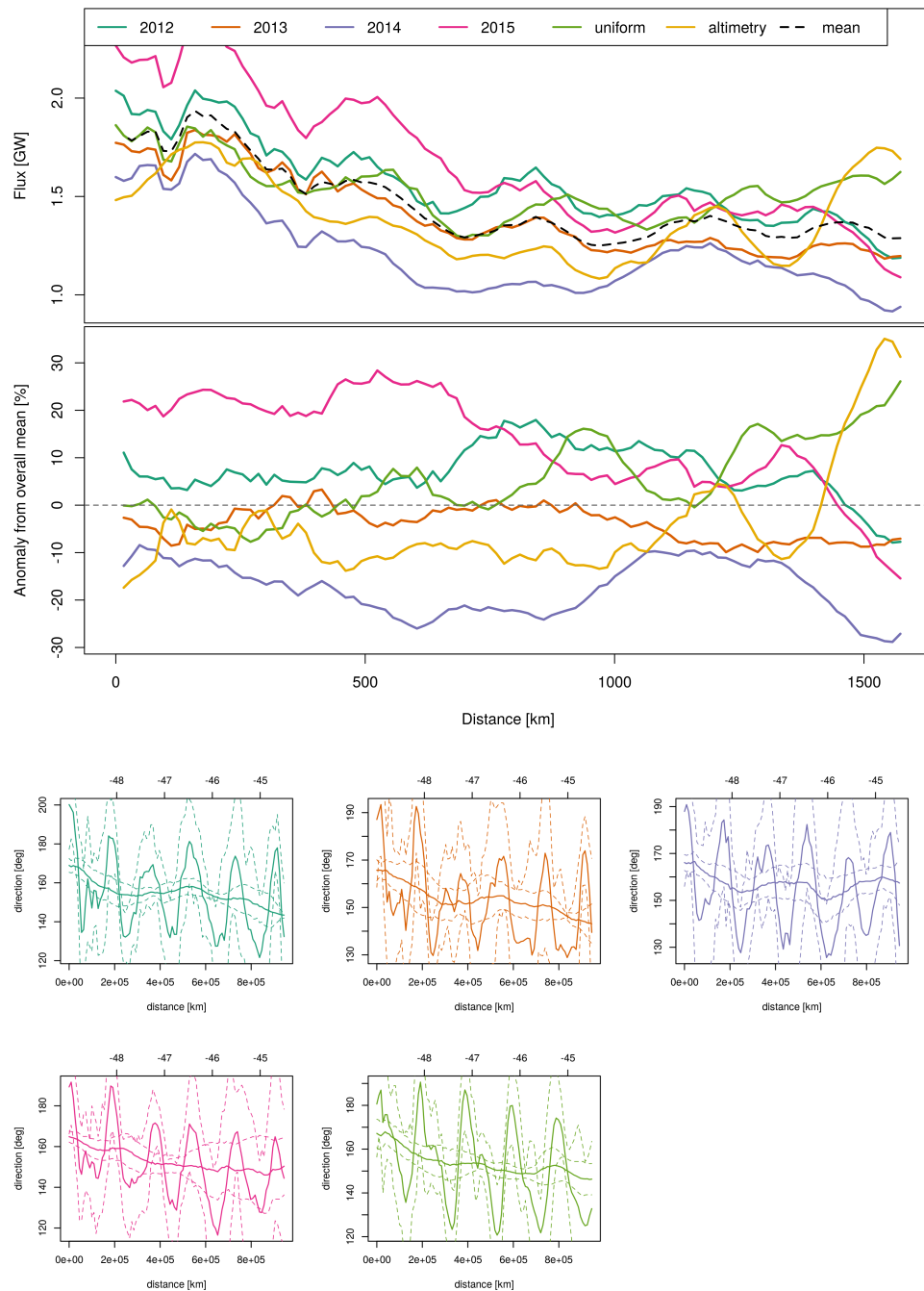
Uniform: Three beams similar to satellite. Central primarily originates in main Macquarie Ridge. There is large variability in the northern, southern, but central is stable.

There two major generation hotspots associated with steep submarine seamounts (Figure 1).

The other region of generation is behind located Campbell Plateau.

Additionally, there is a standing wave. Now we investigate interaction between conversion and standing wave.

Spatial maps of conversion rates show variation in magnitude and location of conversion hotspots (Fig. 1). The energy transfers predominantly occur along steep flanks of two seamounts. The most striking difference was found between '2014' and 'uniform' experi-



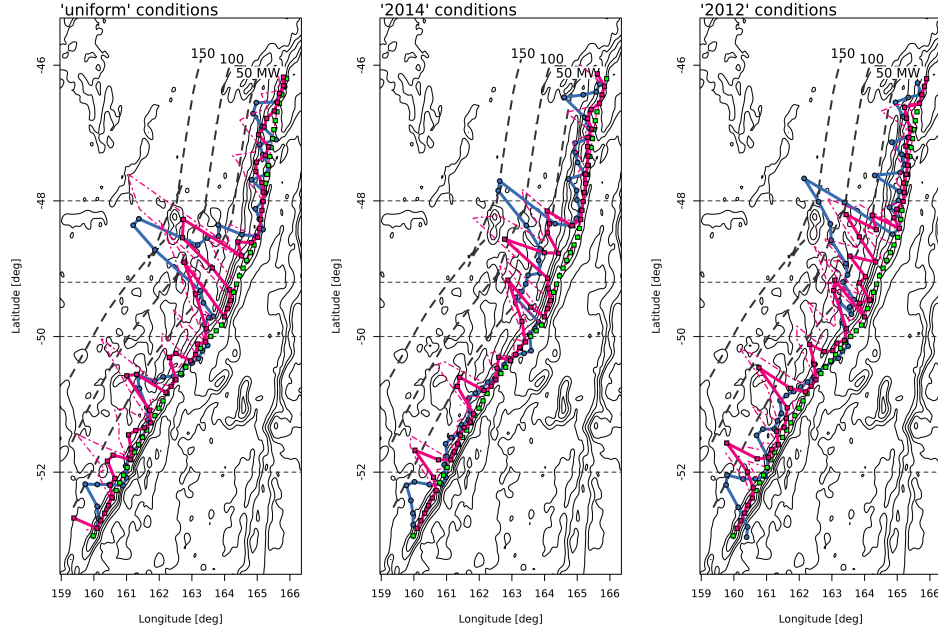


Figure 1: Comparison of inverse solution and numerically diagnosed.

ment.

Conversion rates vary between experiments. Knife edge calculations with WKB-scaled depth does not confirm the same variations (Figure 2).

The other possibility for variations can be seen due to presence of remote waves. Model conversion rates and knife edge, Enhancement of generation due to remote propagating tides.

So variations in standing wave leads to variations in conversion.

4.2 Variation of standing wave, HYCOM

We represent standing wave as interference of two waves (Martini et al. (2007)),

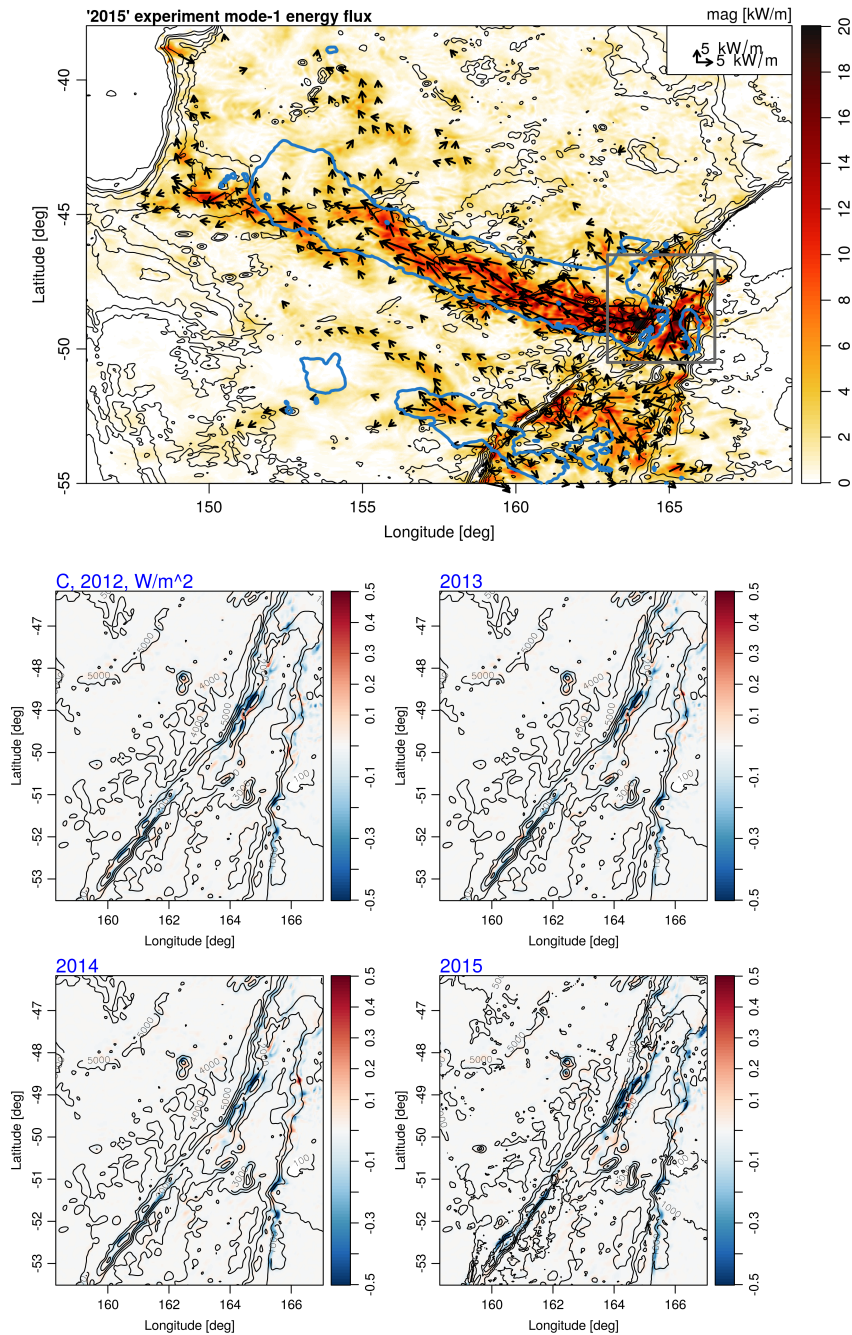


Figure 2: Energy flux map of the beam in Tasman Sea (a) and conversion rates at Macquarie Ridge (b).

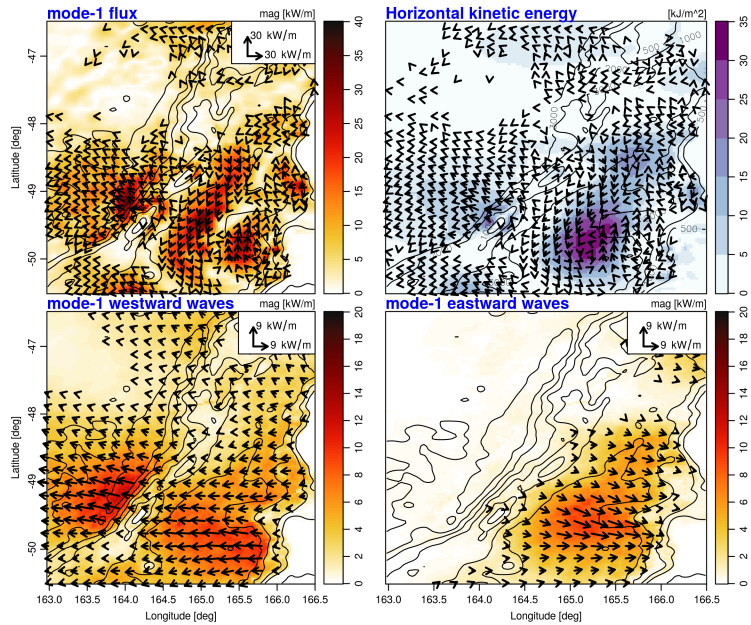


Figure 3: Standing wave

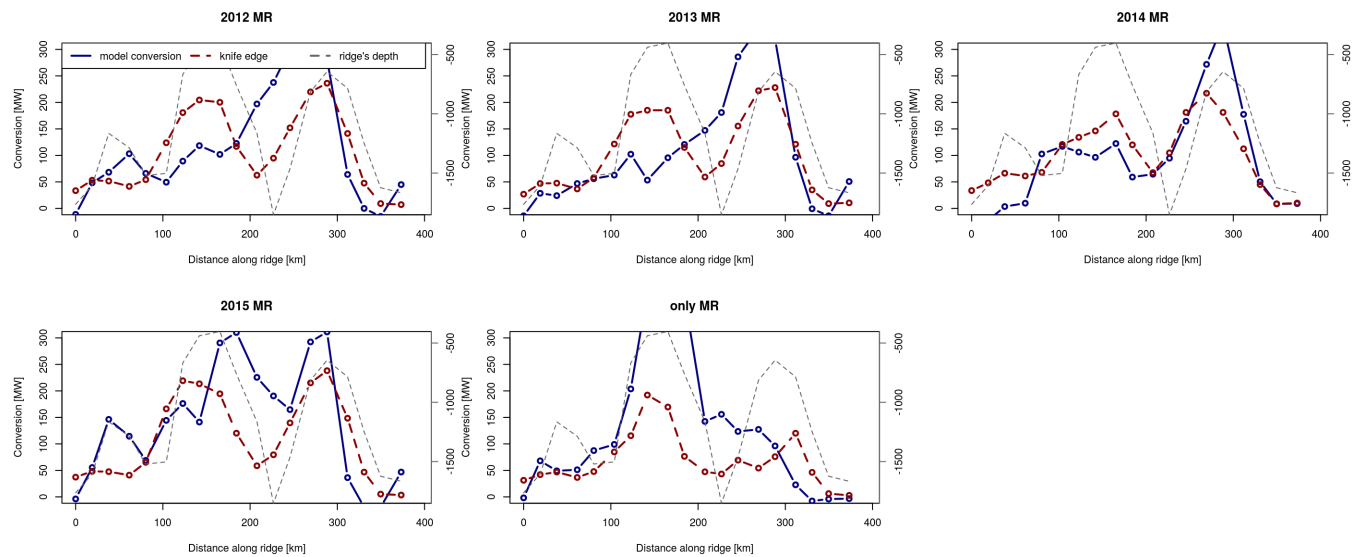


Figure 4: Variation of integrated conversion rates and knife edge

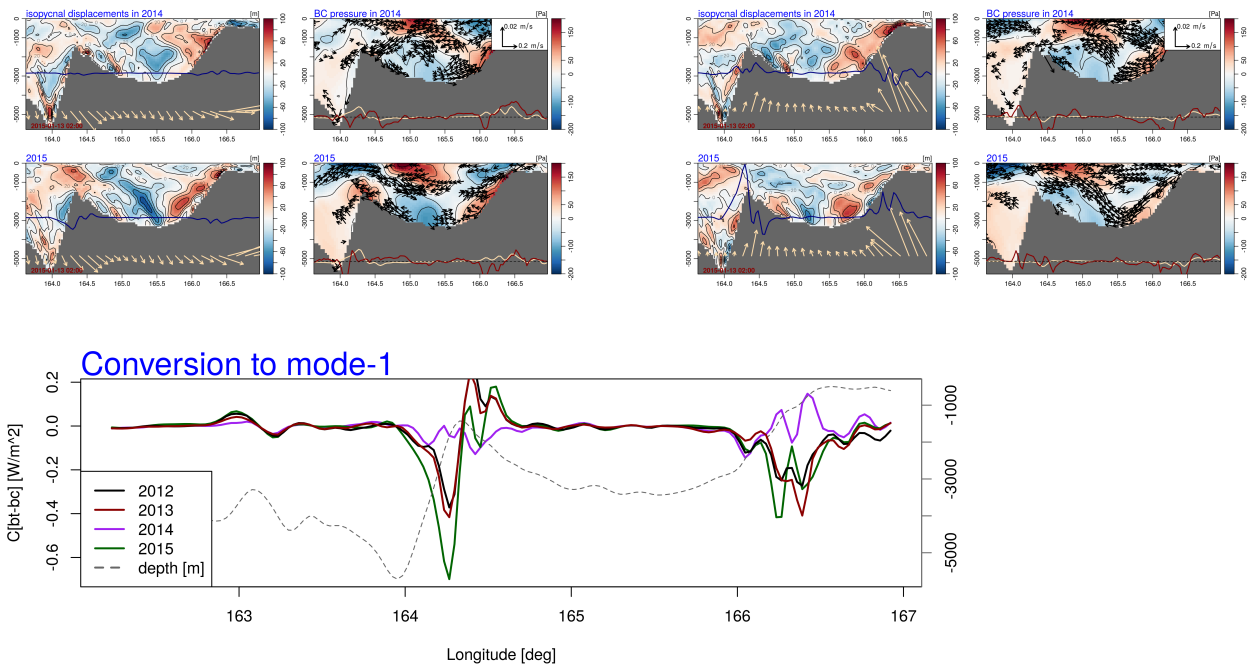
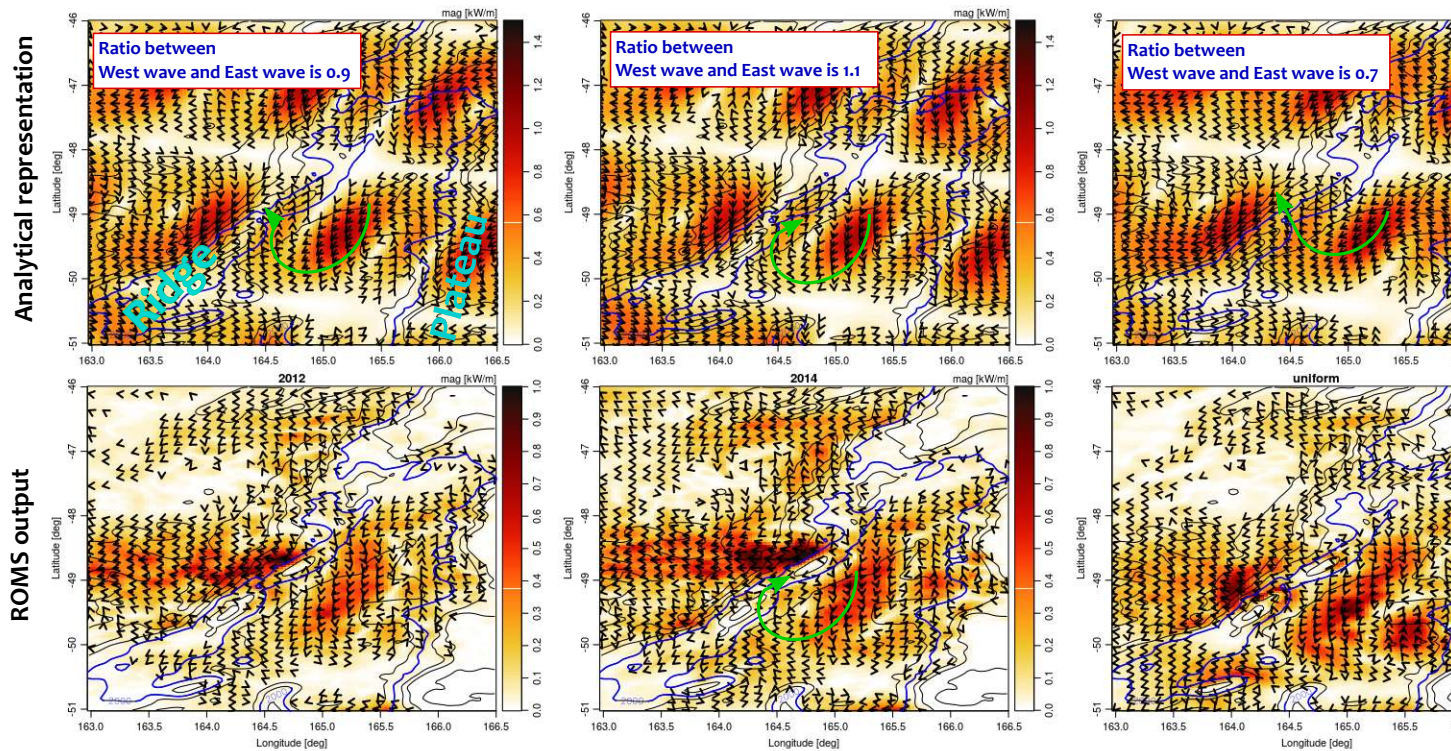
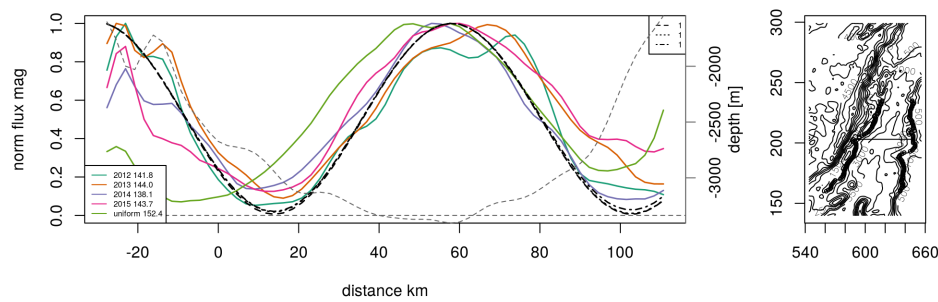


Figure 5: Model output





Discussion on variability of standing wave: stratification?

It was tested hypothesis that the stratification controls, but results are inconclusive.

5 Discussion: Field observations and Boundary condition for scattering

6 Conclusions

Appendices

A Analytical model for knife edge

Let consider a simplified problem of the internal tide generation at a three dimensional ridge. That is generating topography has extent in along x-axis, a , but infinitely small width. We will not pursue full solution of the problem and will not seek actual amplitudes of baroclinic modes, but rather concentrate on defining spatial pattern of the generated waves (might move up to opening). Under such problem statement the actual height is of no importance. And hence, in frame reference traveling with barotropic current, the topography becomes a piston-alike wavemaker that sends out the lowest mode internal tide. Its behavior in flat bottom ocean is well represented by Laplace tidal equations (cf Kelly et al. (2012)):

$$\vec{u}_t + 2\Omega \vec{k} \times \vec{u} = -\frac{1}{\rho_0} \nabla \cdot p \quad (12)$$

$$\nabla \cdot \vec{u} = -\left(\frac{1}{N^2 - \omega^2} p_z\right)_{tz} \quad (13)$$

with boundary conditions on the ridge,

$$\vec{u} \cdot \vec{n}|_{ridge} = \vec{u}_{bt} \cdot \vec{n}|_{ridge} \quad (14)$$

And boundary condition in the infinity implying outgoing waves. Note that barotropic current, in general, is given as a current ellipse written in complex form as $\vec{u}_{bt} = u_{bt} + iv_{bt}$. This means that the boundary condition does not have a simple harmonic form. But the barotropic current can be decomposed to clockwise (CW) and counterclockwise components,

$$\vec{u}_{bt} = W_{CW} e^{-(i\omega t - \phi_{CW})} + W_{CCW} e^{(i\omega t + \phi_{CCW})} \quad (15)$$

and the generation of internal tide can be solved separately for two oppositely rotating currents. In further discussion the only one component (CCW) is taken care of since a

solution will have similar form with differences arising in sign in front of tidal frequency. Considering rigid lid approximation and impermeable bottom equations for eigen modes is solved such that wavelength of corresponding mode is introduced. Then the dynamical equations can be reformulated as Helmholtz equation with harmonic temporal dependence implied and appropriate polarization relations,

$$\nabla^2 p + k_n^2 p = 0 \quad (16)$$

$$u = \frac{-i\omega p_x + fp_y}{\omega^2 - f^2}, \quad v = \frac{-i\omega p_y - fp_x}{\omega^2 - f^2} \quad (17)$$

Since the problem is now formulated in terms of pressure only, boundary condition takes the following form (Greenspan (1968)),

$$\left[\frac{-i\omega p_y - fp_x}{\omega^2 - f^2} \right]_{ridge} = \vec{u}_{BT}|_{ridge} \quad (18)$$

The above equations (5-8) state generation of internal tides by vibrating strip of width a . Such problem was solved for radiation of acoustic waves by Morse and Feshbach (1946). Since in Cartesian coordinates the strip boundary condition does not allow separation of variables, one can employ elliptic coordinate system,

$$x = \frac{a}{2} \cosh \mu \cos \theta, \quad y = \frac{a}{2} \sinh \mu \sin \theta$$

where edges of the strip will be focii of ellipse, boundary condition will take simpler form,

$$\left[\frac{-i\omega p_\mu + fp_\theta}{\omega^2 - f^2} \right]_{\mu=0} = \frac{a}{2} \sin \theta (\vec{u}_{BT}|_{\mu=0}) \quad (19)$$

The factor $\frac{a}{2} \sin \theta$ arises via conversion from Cartesian to elliptical derivatives. Note change of sign for p_{theta} because opposite growth of θ argument to x argument. Laplace operator in the elliptical coordinates has eigensolutions ("sloshing modes") in form of Mathieu functions

(Stratton (2007)) that solution for the emitted waves will have form of,

$$p \sim \sum_j [Se_j, So_j](h, \theta) [Je_j, Jo_j, Ye_j, Yo_j](h, \mu) \quad (20)$$

with Se_j , So_j - angular Mathieu functions of order j corresponding to cos and sin, Je_j , Jo_j and Ye_j , Yo_j - radial Mathieu functions of the first and second kind of order j corresponding to Bessel functions. The physical parameter that sets Mathieu functions behavior is $h = ak_n 4$ so that in large distance limit, $h\mu \gg 1$, $rk_n \gg a$, they will represent circular harmonics.

Now RHS of boundary condition (9) can be expressed in series of Mathieu functions,

$$\sin \theta = \sum_{j=0}^{\infty} C_{2j+1} So_{2j+1}(\theta) \quad (21)$$

with coefficients C_{2j+1} defined by normalization constants $N_{2j+1} = \int_0^{2\pi} So_{2j+1}^2(\theta) d\theta$ and the first Fourier coefficient of So_{2j+1} . The above series for sin and form of the boundary condition suggest solution in the form,

$$p(\mu, \theta) = \sum_{j=0}^{\infty} (A_{2j+1} So_{2j+1}(\theta) + B_{2j+1} Se_{2j+1}(\theta)) Ho_{2j+1}^1(\mu) \quad (22)$$

Here $Ho_{2j+1}^1(\mu) = Jo_{2j+1} + iYo_{2j+1}$ is a Hankel-Mathieu function. For CCW component to ensure condition for outgoing radiation, the sign should be different, so $Ho_{2j+1}^2(\mu) = Jo_{2j+1} - iYo_{2j+1}$.

Now substituting (11, 12) into (9) the unknown coefficients A , B are obtained,

$$(-i\omega (\sum A So + B Se) Ho' + f (\sum A So' + B Se') Ho) = \sum (\omega^2 - f^2) C So$$

At first, multiplying above equation by So_{2m+1} and taking integral from 0 to 2π , so that $\int_0^{2\pi} So_{2m+1} Se_{2j+1} d\theta = \int_0^{2\pi} So'_{2j+1} So_{2m+1} d\theta = 0$, $\int_0^{2\pi} So_{2m+1} So_{2m+1} d\theta = No_{2m+1}$, $\int_0^{2\pi} So_{2m+1} Se'_{2j+1} d\theta = -N'_{2j+1}^{2m+1}$. In the last statement orthogonality between So and Se' is not satisfied. Equation

on each order is obtained

$$(-i\omega A_{2m+1} No_{2m+1}^o Ho'_{2m+1} + f \sum_j B_{2j+1} Noe'^{2m+1}_{2j+1} Ho_{2j+1}) = C No_{2m+1} \quad (23)$$

And at second, carrying out the same procedure but with Se_{2j+1} ,

$$(-i\omega B_{2m+1} Ne_{2m+1} Ho'_{2m+1} + f \sum_j A_{2j+1} Noe'^{2m+1}_{2j+1} Ho_{2j+1}) = 0 \quad (24)$$

Note that $\int_0^{2\pi} Se'_{2j+1} So_{2m+1} d\theta = - \int_0^{2\pi} So'_{2j+1} Se_{2m+1} d\theta$, i.e. $Noe'^{2m+1}_{2j+1} = -(Noe'^{2m+1}_{2j+1})^T$.

Equations (13) and (14) form a linear system to find coefficients for different component of the total field. These equations are solved numerically with $j_{max} = 5$ due to rapid convergence of the involved series.

B Inverse model

The model closely follows ideas used in ref-to-Luc, 2010 and -Jody-2016. The internal tide generating ridge is given by point sources each emitting following

$$p = p_0 \frac{2}{\pi k d} \cdot e^{ikd} \quad (25)$$

where k - wavenumber associated with eigen mode-1, i.e. $k = \sqrt{\omega^2 - f^2} c_{eigen}^2$, d - distance between a point source and an observation point. By observation points here and after is meant points in which observations are inverted. The given solution is a solution of pressure disturbance propagation for two dimensional wave equation (p. 22, Frisk) and describes outgoing cylindrical wave. This is a far field approximation ($kd \ll 1$), in the near source zone the solution is substituted by Hankel functions. Here representation is simplified and observation points on the distance less than wavelength are omitted. Though introduction of Hankel function into the inverse model does not involve any additional complexity. By pressure here is thought mode-1 pressure amplitude that can be connected to sea level

disturbance or isopycnal displacements.

To describe energy fluxes in the observational points polarization relations for cylindrical Poincare wave are invoked,

$$u = \frac{p_0}{\rho_{const}} * \frac{-i\omega \cos(\theta) + f \sin(\theta)}{\omega^2 - f^2} \cdot p_{\vec{d}} \quad (26)$$

$$v = \frac{p_0}{\rho_{const}} * \frac{-i\omega \sin(\theta) - f \cos(\theta)}{\omega^2 - f^2} \cdot p_{\vec{d}} \quad (27)$$

where $p_{\vec{d}}$ is a derivative along radius-vector \vec{d} ,

$$p_{\vec{d}} = (i \cdot k - \frac{1}{2\vec{d}})p \quad (28)$$

In further description of the inverse model it is used following notation, indices i, k define i, k -th point sources, while j - j -th observation point.

The tidally and depth averaged energy fluxes will be given as an interference of pointwise fields from all sources,

$$F_j^x = \frac{1}{2} \sum_k u_{kj}^* \sum_i p_{ij} \int_H^0 \psi_1(z)^2 dz \quad (29)$$

$$F_j^y = \frac{1}{2} \sum_k v_{kj}^* \sum_i p_{ij} \int_H^0 \psi_1(z)^2 dz \quad (30)$$

Note different indexes for u/v and p meaning that cross multiplication is involved which leads to complex interference pattern. In energy flux formulation normalization coefficient associated with eigenmode structure function are introduced by corresponding mode-1 structure function, $\psi_1(z)$. Coefficient $1/2$ is used for convenience to convert actual time averaging involved to multiplication of complex numbers. In further description the constant coefficients are omitted due to their irrelevance. The previous relations can be expressed in matrix

form (it is not fully correct for fluxes, multiplication is done term by term per point),

$$p_j = B_{ji}^p p_i, \quad u_j = B_{ji}^u p_i, \quad v_j = B_{ji}^v p_i \quad (31)$$

$$F_j^x = (B_{jk}^u p_k)^* B_{ji}^p p_i, \quad F_j^y = (B_{jk}^v p_k)^* B_{ji}^p p_i \quad (32)$$

where tensor notation is used, i.e. summation is done over same indices. Matrices B_{ij}^p , B_{ij}^u , B_{ij}^v are short notation for generaion model and polarization relations, for example,

$$B_{ji}^p = p_i \frac{2}{\pi k d_j} \cdot e^{ikd_j} \quad (33)$$

These can be thought as discretization of operators transforming distribution of sources into interference pattern in pressure and velocity fields.

Apparently, the energy flux relations are non-linear. To deal with this it is proposed an iterative technique. Let at m -th iteration there is a known distribution of wave amplitude at sources, p_i^m , the total energy flux field can be reconstruced by (32). Than it is desired to find a small adjustment δp_i^m (“nudge factor”) such that residual between observed field and analytical description will be decreased. One can write,

$$\begin{aligned} F_j^x &= (B_{jk}^u(p_k^m + \delta p_k^m))^* B_{ji}^p(p_i^m + \delta p_i^m) = \\ &= (B_{jk}^u p_k^m)^* B_{ji}^p p_i^m + (B_{jk}^u \delta p_k^m)^* B_{ji}^p p_i^m + (B_{jk}^u p_k^m)^* B_{ji}^p \delta p_i^m + (B_{jk}^u \delta p_k^m)^* B_{ji}^p \delta p_i^m \\ F_j^x - (B_{jk}^u p_k^m)^* B_{ji}^p p_i^m &= (B_{jk}^u \delta p_k^m)^* B_{ji}^p p_i^m + (B_{jk}^u p_k^m)^* B_{ji}^p \delta p_i^m + (B_{jk}^u \delta p_k^m)^* B_{ji}^p \delta p_i^m \end{aligned} \quad (34)$$

The left hand side of (34) represents the residual, the right hand side sets a controlling equation to obtain adjustment neceassary to decrease the residual. The last term of RHS shows a non-linear nature of the problem. This is omitted since the purpose of consequent iterative technique is to find the final source distribution such that the model equations (32)

are satisfied in least square sense. Than the “nudge-factor” can be found as inverse of

$$F_j^x - (B_{jk}^u p_k^m)^* B_{ji}^p p_i^m = R_j^x = \left[(B_{jk}^u)^* B_{ji}^p p_i^m + (B_{jk}^u p_k^m)^* B_{ji}^p \right] \delta p_i^m \quad (35)$$

(these equations are not in matrix form, but obsevation point by observation point). Hence, the aim of inverse model is to decrease error in representation of energy fluxes. The equation (35) can be solved separately for zonal and meridional fluxes and also simultaneously for both directions. That is at each iteration step the nudge-factor is found first for zonal, than for meridional direction and finally, for both simultaneously. At the end pressure distribution is changed by average from all three substeps.

Note the inverse model equation (35) is supported by additional condition stating that amplitude is nonnegative, $p_i^m + \delta p_i^m \geq 0$. All of this numerically is solved by linear programming routine lsei (least square with inequality) provided by LINPACK package.

Here it will be presented a test convergence and number tests on robustness on proposed iterative inverse model. The initial flux field is given by Fig. ?? where by crosses are shown observational points. This define prescribed F_j^x or F_j^y . Note that the prescribed field aims to describe midbasin energy flux field with Tasman shelf ommitted due to presence of reflection and complex bathymetry. The point sources distribution are given by green dots and at the first iteration step are set to $p_i^0 = 100Pa$. The distribution of points sources is representative to distribution of steep bathymetry which is belived to be an internal tide generator. In the inverse model there are only two parameters that describe characteristic of the internal tide, wavenumber and normalization coefficients used in energy flux. Both are found from solving eigenvalue for randomly picked stratification profile. This result in wavelength of 180 km which is a representative value for Tasman Sea conditions. In the same way eigenfunctions are obtained and normalization coefficients are found.

Hence, the inverse model does not account for

1. Bathymetry variation

2. Stratification variability
3. Variation of barotropic tide along ridges

The first two points are thought to have minor effect on internal tidal beam structure. While the third is omitted to preserve simplicity of generation model. Additional tests were done with variation in barotropic tide phase along ridges, but they did not bring any substantial changes in foregoing results.

To show convergence of the inverse model it is given change in pressure amplitude with each iteration. Here convergence is defined by

$$Conv = \sum_i \frac{(p_i^m - p_i^{m-1})^2}{(0.5 \cdot (p_i^m + p_i^{m-1}))^2}$$

The iterative solver is stopped when convergence is reaching tolerance. Here it is set to 0.01. From Figure (2a) it is seen that by 17th iteration there is no appreciable change in the inverse solution. This means that influence of non-linear terms in (34) became negligible and the distribution of amplitude along the source region is the best in least square sense. The error of such description is given on subsequent panels of Fig. 2, where root-mean-square-error for different energy flux parameters is defined for example zonal component as

$$E_x = \sqrt{\frac{\sum_{obs} (F_i^x - \hat{F}_i^x)^2}{N_{obs}}} \quad (36)$$

As it is seen the error is approaching stability for all used components much faster than convergence in amplitude. Note that the error is larger in zonal fluxes. The inverse solution can not predict far field behavior which is believed due to interaction with East Tasman Plateau. The obtained solution is given by Fig. 3. Here it is found that the inverse solution can not well represent the beam close to East Tasman Plateau. The following reasons can be named: interaction with topography and inadequacy of cylindrical wave model in the far-far field. It is believed that the second reason is the main. In general, the inverse solution picks

up the central beam pretty well, outlines its boundary and the major region is satisfying manner. As well note that the northern and southern beams are also found in the solution.

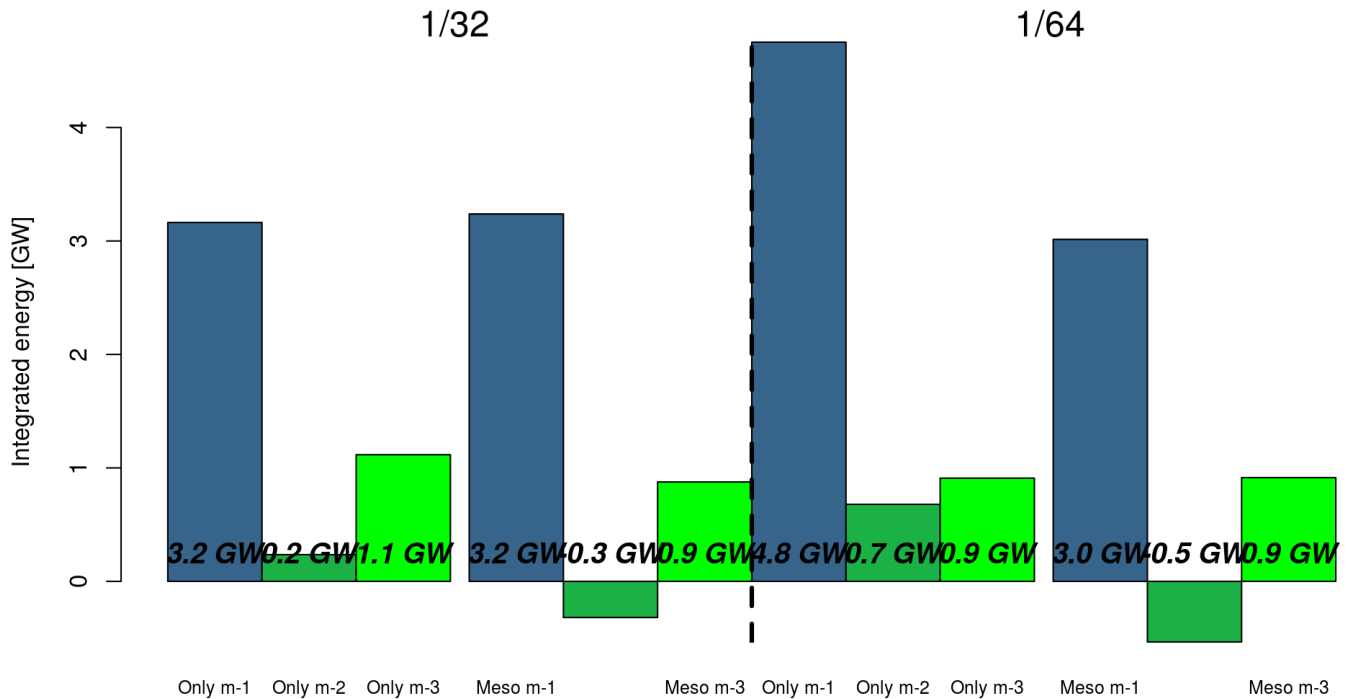


Figure 6: Change in energetics of the beam.

A Figures

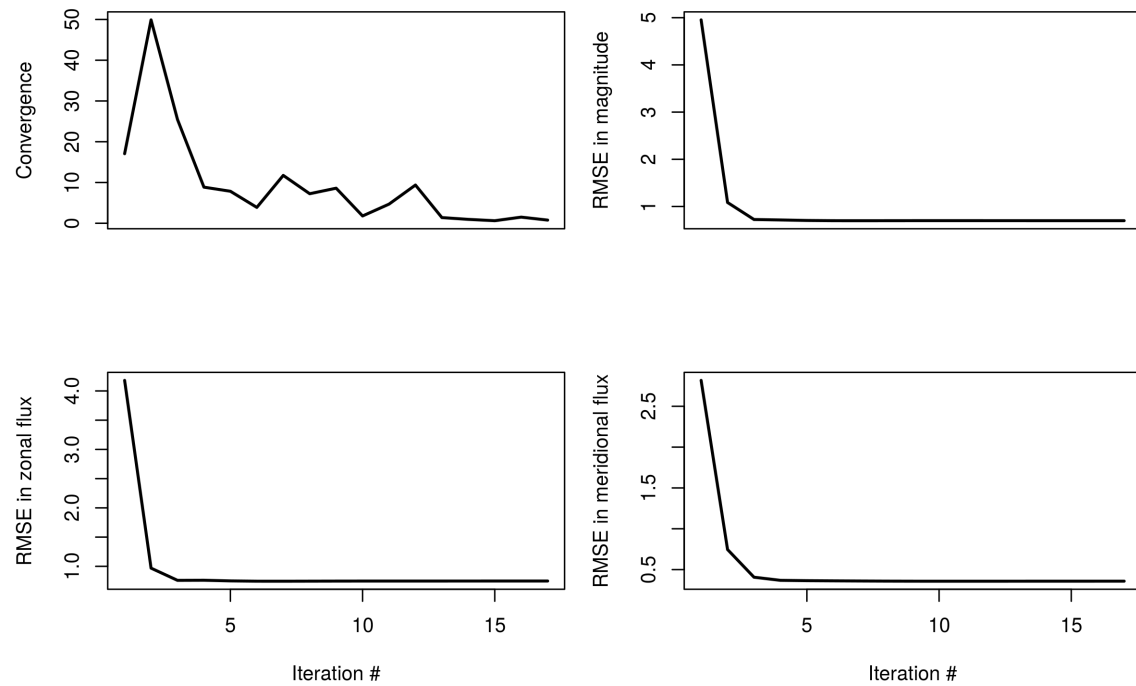


Figure 7: Convergence

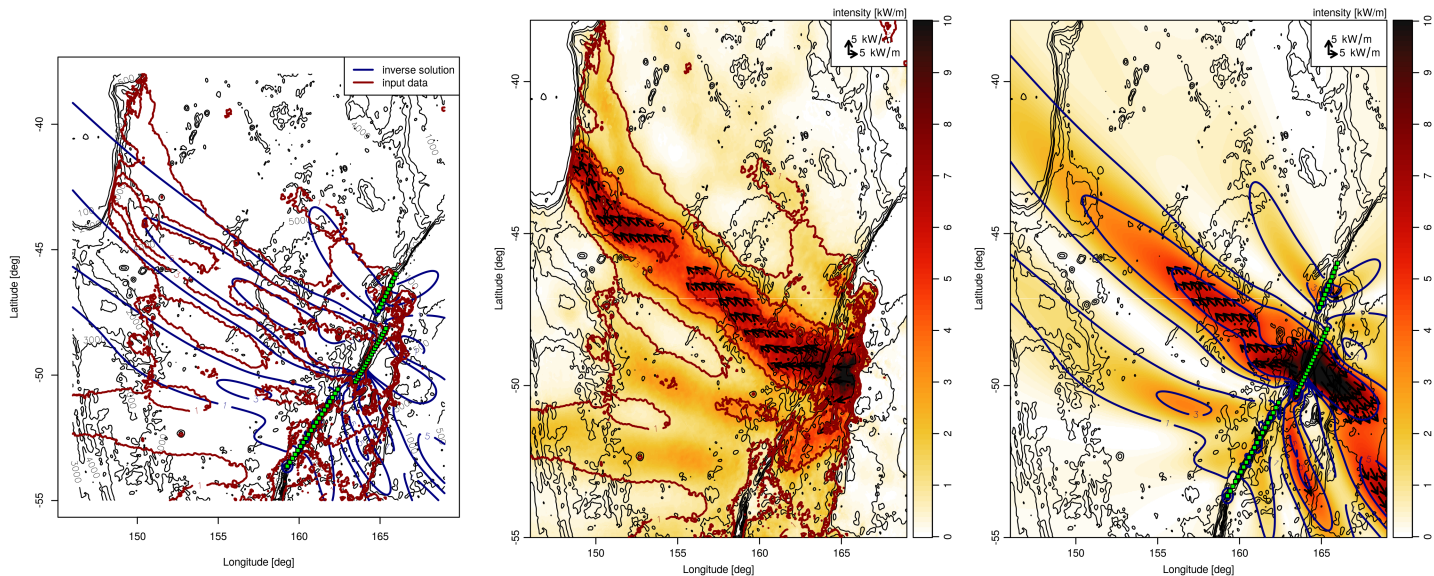


Figure 8: Left panel - Overlaid isolines of energy flux magnitude of magnitude 1, 3, 5 kW/m. Middle panel - input data. Right panel - inverse solution.

TO DO LIST

- Polish: Clin and energy budget, knife edge, WKB-stretching, standing wave
- Inverse model, elliptic waves are the way to go, why the phase can not be planar over much smaller stripes, something wrong with formulation of generation problem. See acoustics paper.
- Why in new experiments the beam did not move?
- Reasons for incoherence?
- Is there going to be any seasonal cycle?

References

Ansorg, J. K., Arbic, B. K., Alford, M. H., Buijsman, M. C., Shriver, J. F., Zhao, Z., Richman, J. G., Simmons, H. L., Timko, P. G., Wallcraft, A. J., et al. (2017). Semidiurnal internal tide energy fluxes and their variability in a global ocean model and moored observations. *Journal of Geophysical Research: Oceans*, 122(3):1882–1900.

Buijsman, M., Uchiyama, Y., McWilliams, J., and Hill-Lindsay, C. (2012a). Modeling semidiurnal internal tide variability in the southern California bight. *Journal of Physical Oceanography*, 42(1):62–77.

Buijsman, M. C., Klymak, J. M., Legg, S., Alford, M. H., Farmer, D., MacKinnon, J. A., Nash, J. D., Park, J.-H., Pickering, A., and Simmons, H. (2014). Three-dimensional double-ridge internal tide resonance in Luzon Strait. *Journal of Physical Oceanography*, 44(3):850–869.

Buijsman, M. C., Legg, S., and Klymak, J. (2012b). Double-ridge internal tide interference and its effect on dissipation in Luzon Strait. *Journal of Physical Oceanography*, 42(8):1337–1356.

- Carter, G., Merrifield, M., Becker, J., Katsumata, K., Gregg, M., Luther, D., Levine, M., Boyd, T. J., and Firing, Y. (2008). Energetics of m 2 barotropic-to-baroclinic tidal conversion at the hawaiian islands. *Journal of Physical Oceanography*, 38(10):2205–2223.
- Chavanne, C., Flament, P., Luther, D., and Gurgel, K. (2010). The surface expression of semidiurnal internal tides near a strong source at hawaii. part ii: Interactions with mesoscale currents*. *Journal of Physical Oceanography*, 40(6):1180–1200.
- Cummins, P. F. and Oey, L.-Y. (1997). Simulation of barotropic and baroclinic tides off northern british columbia. *Journal of Physical Oceanography*, 27(5):762–781.
- Di Lorenzo, E., Young, W. R., and Smith, S. L. (2006). Numerical and analytical estimates of m 2 tidal conversion at steep oceanic ridges. *Journal of physical oceanography*, 36(6):1072–1084.
- Dunphy, M. and Lamb, K. G. (2014). Focusing and vertical mode scattering of the first mode internal tide by mesoscale eddy interaction. *Journal of Geophysical Research: Oceans*, 119(1):523–536.
- Dunphy, M., Ponte, A. L., Klein, P., and Le Gentil, S. (2017). Low-mode internal tide propagation in a turbulent eddy field. *Journal Of Physical Oceanography*, 47(3):649–665.
- Dushaw, B. D. (2002). Mapping low-mode internal tides near hawaii using topex/poseidon altimeter data. *Geophysical Research Letters*, 29(8).
- Echeverri, P. and Peacock, T. (2010). Internal tide generation by arbitrary two-dimensional topography. *Journal of Fluid Mechanics*, 659:247–266.
- Egbert, G. and Ray, R. (2000). Significant dissipation of tidal energy in the deep ocean inferred from satellite altimeter data. *Nature*, 405(6788):775–778.
- Egbert, G. D. and Erofeeva, S. Y. (2002). Efficient inverse modeling of barotropic ocean tides. *Journal of Atmospheric and Oceanic Technology*, 19(2):183–204.

- Garrett, C. and Kunze, E. (2007). Internal tide generation in the deep ocean. *Annu. Rev. Fluid Mech.*, 39:57–87.
- Greenspan, H. P. (1968). *The theory of rotating fluids*. CUP Archive.
- Haidvogel, D. B. and Beckmann, A. (1999). *Numerical ocean circulation modeling*. World Scientific.
- Hansen, P. C. (1999). The l-curve and its use in the numerical treatment of inverse problems.
- Hansen, P. C. and OLeary, D. P. (1993). The use of the l-curve in the regularization of discrete ill-posed problems. *SIAM Journal on Scientific Computing*, 14(6):1487–1503.
- Hendry, R. (1977). Observations of the semidiurnal internal tide in the western north atlantic ocean. *Philosophical Transactions of the Royal Society of London A: Mathematical, Physical and Engineering Sciences*, 286(1330):1–24.
- Holloway, P. E. and Merrifield, M. A. (1999). Internal tide generation by seamounts, ridges, and islands. *Journal of Geophysical Research: Oceans*, 104(C11):25937–25951.
- Kang, D. and Fringer, O. (2012). Energetics of barotropic and baroclinic tides in the monterey bay area. *Journal of Physical Oceanography*, 42(2):272–290.
- Kelly, S. and Nash, J. (2010). Internal-tide generation and destruction by shoaling internal tides. *Geophysical Research Letters*, 37(23).
- Kelly, S., Nash, J., and Kunze, E. (2010). Internal-tide energy over topography. *Journal of Geophysical Research: Oceans (1978–2012)*, 115(C6).
- Kelly, S. M. and Lermusiaux, P. F. (2016). Internal-tide interactions with the gulf stream and middle atlantic bight shelfbreak front. *Journal of Geophysical Research: Oceans*, 121(8):6271–6294.

- Kelly, S. M., Nash, J. D., Martini, K. I., Alford, M. H., and Kunze, E. (2012). The cascade of tidal energy from low to high modes on a continental slope. *Journal of Physical Oceanography*, 42(7):1217–1232.
- Kerry, C. G., Powell, B. S., and Carter, G. S. (2013). Effects of remote generation sites on model estimates of m 2 internal tides in the philippine sea*. *Journal of Physical Oceanography*, 43(1):187–204.
- Kerry, C. G., Powell, B. S., and Carter, G. S. (2016). Quantifying the incoherent m2 internal tide in the philippine sea. *Journal of Physical Oceanography*, 46(8):2483–2491.
- Kunze, E., Rosenfeld, L. K., Carter, G. S., and Gregg, M. C. (2002). Internal waves in monterey submarine canyon. *Journal of Physical Oceanography*, 32(6):1890–1913.
- Kurapov, A. L., Egbert, G. D., Allen, J., Miller, R. N., Erofeeva, S. Y., and Kosro, P. (2003). The m 2 internal tide off oregon: Inferences from data assimilation. *Journal of Physical Oceanography*, 33(8):1733–1757.
- Long, R. B. (1986). Inverse modeling in ocean wave studies. In *Wave dynamics and radio probing of the ocean surface*, pages 571–593. Springer.
- Longuet-Higgins, M. S. (1961). Observations of the directional spectrum of sea waves using the motions of a floating buoy. *Ocean wave spectra*, pages 111–136.
- Lozovatsky, I. D., Morozov, E. G., and Fernando, H. (2003). Spatial decay of energy density of tidal internal waves. *Journal of Geophysical Research: Oceans*, 108(C6).
- Martini, K., Alford, M., Nash, J., Kunze, E., and Merrifield, M. (2007). Diagnosing a partly standing internal wave in mamala bay, oahu. *Geophysical Research Letters*, 34(17).
- Merrifield, M. A. and Holloway, P. E. (2002). Model estimates of m2 internal tide energetics at the hawaiian ridge. *Journal of Geophysical Research: Oceans*, 107(C8).

- Merrifield, M. A., Holloway, P. E., and Johnston, T. (2001). The generation of internal tides at the hawaiian ridge. *Geophysical Research Letters*, 28(4):559–562.
- Mooers, C. N. (1975). Several effects of baroclinic currents on the three-dimensional propagation of inertialinternal waves. *Geophysical Fluid Dynamics*, 6(3):277–284.
- Morse, P. M. and Feshbach, H. (1946). *Methods of theoretical physics*. Technology Press.
- Müller, P. and Liu, X. (2000). Scattering of internal waves at finite topography in two dimensions. part i: Theory and case studies. *Journal of physical oceanography*, 30(3):532–549.
- Munk, W. (1997). Once again: once againtidal friction. *Progress in Oceanography*, 40(1):7–35.
- Munk, W., Worcester, P., and Wunsch, C. (2009). *Ocean acoustic tomography*. Cambridge University Press.
- Munk, W. H., Miller, G., Snodgrass, F., and Barber, N. (1963). Directional recording of swell from distant storms. *Philosophical Transactions of the Royal Society of London A: Mathematical, Physical and Engineering Sciences*, 255(1062):505–584.
- Munroe, J. and Lamb, K. (2005). Topographic amplitude dependence of internal wave generation by tidal forcing over idealized three-dimensional topography. *Journal of Geophysical Research: Oceans*, 110(C2).
- Osborne, J., Kurapov, A., Egbert, G., and Kosro, P. (2011). Spatial and temporal variability of the m 2 internal tide generation and propagation on the oregon shelf. *Journal of Physical Oceanography*, 41(11):2037–2062.
- Park, J.-H. and Watts, D. R. (2006). Internal tides in the southwestern japan/east sea. *Journal of Physical Oceanography*, 36(1):22–34.

- Pickering, A., Alford, M., Nash, J., Rainville, L., Buijsman, M., Ko, D. S., and Lim, B. (2015). Structure and variability of internal tides in luzon strait*. *Journal of Physical Oceanography*, 45(6):1574–1594.
- Rainville, L., Johnston, T. S., Carter, G. S., Merrifield, M. A., Pinkel, R., Worcester, P. F., and Dushaw, B. D. (2010). Interference pattern and propagation of the m 2 internal tide south of the hawaiian ridge. *Journal of Physical Oceanography*, 40(2):311–325.
- Rainville, L. and Pinkel, R. (2006). Propagation of low-mode internal waves through the ocean. *Journal of physical oceanography*, 36(6):1220–1236.
- Rienecker, M. M., Suarez, M. J., Gelaro, R., Todling, R., Bacmeister, J., Liu, E., Bosilovich, M. G., Schubert, S. D., Takacs, L., Kim, G.-K., et al. (2011). Merra: Nasas modern-era retrospective analysis for research and applications. *Journal of climate*, 24(14):3624–3648.
- Shchepetkin, A. F. and McWilliams, J. C. (2005). The regional oceanic modeling system (roms): a split-explicit, free-surface, topography-following-coordinate oceanic model. *Ocean modelling*, 9(4):347–404.
- Simmons, H. L., Hallberg, R. W., and Arbic, B. K. (2004). Internal wave generation in a global baroclinic tide model. *Deep Sea Research Part II: Topical Studies in Oceanography*, 51(25):3043–3068.
- Stratton, J. A. (2007). *Electromagnetic theory*. John Wiley & Sons.
- Terker, S. R., Girton, J. B., Kunze, E., Klymak, J. M., and Pinkel, R. (2014). Observations of the internal tide on the california continental margin near monterey bay. *Continental Shelf Research*, 82:60–71.
- Walters, R. A., Goring, D. G., and Bell, R. G. (2001). Ocean tides around new zealand. *New Zealand Journal of Marine and Freshwater Research*, 35(3):567–579.

- Williams, E. G. (2001). Regularization methods for near-field acoustical holography. *The Journal of the Acoustical Society of America*, 110(4):1976–1988.
- Wunsch, C. (1975). Internal tides in the ocean. *Reviews of Geophysics*, 13(1):167–182.
- Xing, J. and Davies, A. M. (1998). A three-dimensional model of internal tides on the malin-hebrides shelf and shelf edge. *Journal of Geophysical Research: Oceans*, 103(C12):27821–27847.
- Zaron, E. D. and Egbert, G. D. (2014). Time-variable refraction of the internal tide at the hawaiian ridge. *Journal of Physical Oceanography*, 44(2):538–557.
- Zhang, Z., Fringer, O., and Ramp, S. (2011). Three-dimensional, nonhydrostatic numerical simulation of nonlinear internal wave generation and propagation in the south china sea. *Journal of Geophysical Research: Oceans*, 116(C5).
- Zhao, Z., Alford, M. H., Girton, J. B., Rainville, L., and Simmons, H. L. (2016). Global observations of open-ocean mode-1 m₂ internal tides. *Journal of Physical Oceanography*, 46(6):1657–1684.
- Zhao, Z., Alford, M. H., MacKinnon, J. A., and Pinkel, R. (2010). Long-range propagation of the semidiurnal internal tide from the hawaiian ridge. *Journal of Physical Oceanography*, 40(4):713–736.
- Zilberman, N., Merrifield, M., Carter, G., Luther, D., Levine, M., and Boyd, T. J. (2011). Incoherent nature of m₂ internal tides at the hawaiian ridge. *Journal of Physical Oceanography*, 41(11):2021–2036.